Available online at www.sciencedirect.com
SCIENCE DIRECT®
Journal of Magnetic Resonance 175 (2005) 21–29
JMR Journal of Magnetic Resonance
www.elsevier.com/locate/jmr

Solid-state ^{27}Al MRI and NMR thermometry for catalytic applications with conventional (liquids) MRI instrumentation and techniques

Igor V. Koptyug [a,*], Dmitry R. Sagdeev [a], Edo Gerkema [b], Henk Van As [b], Renad Z. Sagdeev [a]

[a] International Tomography Center, 3A Institutskaya St., Novosibirsk 630090, Russia
[b] Laboratory of Biophysics and Wageningen NMR Centre, Wageningen University, Dreijenlaan 3, 6703 HA Wageningen, The Netherlands

Received 1 December 2004; revised 1 March 2005
Available online 8 April 2005

Abstract

Multidimensional images of Al_2O_3 pellets, cordierite monolith, glass tube, polycrystalline V_2O_5 and other materials have been detected by ^{27}Al, ^{51}V, and ^{23}Na NMR imaging using techniques and instrumentation conventionally employed for imaging of liquids. These results demonstrate that, contrary to the widely accepted opinion, imaging of "rigid" solids does not necessarily require utilization of solid state NMR imaging approaches, pulse sequences and hardware even for quadrupolar nuclei which exhibit line widths in excess of 100 kHz, such as ^{51}V in polycrystalline V_2O_5. It is further demonstrated that both ^{27}Al NMR signal intensity and spin-lattice relaxation time decrease with increasing temperature and thus can potentially serve as temperature sensitive parameters for spatially resolved NMR thermometry.

Keywords: NMR imaging of solids; ^{27}Al and ^{51}V MRI; Quadrupolar nuclei; Catalyst support; NMR thermometry

1. Introduction

The last decade has witnessed an increasing interest in applying NMR imaging (MRI) to solve problems in chemical and process engineering and related disciplines [1–4]. The driving force behind this is the realization and appreciation of the versatility of the MRI toolkit with its ever growing power to characterize the properties of materials and reactors (structure, morphology, bed packing, porosity, permeability, tortuosity of porous media, etc.) and various mass transport processes within them (flow, filtration, dispersion, and diffusion). While most of the MRI work is based on the detection of the NMR signals of liquids, the possibility to study gas distribution and transport has been demonstrated as well [2]. Nevertheless, the existing MRI toolkit still lacks some of the tools essential for studying multiphase reactors. This includes the ability to image the solid phase in multiphase reactors and processes, and to monitor heat transport in an operating reactor by evaluating local temperatures.

High molecular mobility of liquids and gases assures an averaging of anisotropic interactions of nuclear spins and often leads to the narrowing of an NMR resonance by several orders of magnitude as compared to solids. As a result, the decay of transverse magnetization is slow and the observable signal lasts long enough to avoid problems associated with receiver dead time, fast gradient switching, and sensitivity. Furthermore, relatively low magnetic field gradients are needed to overcome the reduced line broadening. These are the

* Corresponding author. Fax: +7 3832 331399.
E-mail address: koptyug@tomo.nsc.ru (I.V. Koptyug).

1090-7807/$ - see front matter © 2005 Elsevier Inc. All rights reserved.
doi:10.1016/j.jmr.2005.03.005

reasons why the majority of MRI experiments including microimaging studies utilize ^{1}H NMR signal of liquid or liquid-like phases and "soft" solid materials with moderate (100 Hz–3 kHz) line widths such as polymers and elastomers [5–7].

In contrast, MRI of rigid solids [8–10] is hampered to a significant extent due to the fact that low molecular mobility and anisotropic interactions lead to very broad NMR resonances (hundreds of kilohertz and more). This is especially true for MRI of quadrupolar ($I > 1/2$) nuclei for which quadrupolar broadening effects can easily lead to line widths in excess of 1 MHz. While examples of MRI applications to the studies of quadrupolar nuclei have been published in the literature (vide infra), MRI of rigid solids has not by now become a routine technique, mostly, it appears, because such experiments are usually associated with the utilization of specialized hardware, sophisticated pulse sequences and very large magnetic field gradients.

The development of the strategies for routine MRI studies of solids can be very useful for chemical and process engineering, and for catalytic applications in particular. First of all, this would allow the direct imaging of the solid phase in multiphase systems, including the elucidation of the structure of packed beds and structured reactors, which in certain cases can be preferable to imaging voids flooded with liquid. At the same time, image contrast manipulation could provide access to a variety of properties of the solid phase. In particular, the characteristics of the NMR signal of a solid matrix (e.g., catalyst support) can possibly be useful in evaluating local temperatures, a prerequisite for assessing heat transport under reactive conditions. The results reported below demonstrate that such applications are feasible and can be implemented on commercially available microimaging instruments using conventional two-pulse spin–echo sequences.

2. Experimental

All imaging experiments were performed on a Bruker Avance DRX 300 MHz wide bore spectrometer equipped with imaging accessories at 78.2 MHz (^{27}Al), 78.94 MHz (^{51}V) and 79.39 MHz (^{23}Na). For ^{27}Al, ^{23}Na, and ^{51}V imaging experiments, we used the broadband rf probe supplied with the instrument for high resolution NMR spectroscopy. The probe has a saddle-shape rf coil with 6 mm inner diameter which sets the upper limit on the diameter of samples that can be imaged. Fortunately, this broadband probe has the right diameter to fit into the gradient-coils set of the microimaging accessory (micro-2.5, Bruker). For imaging studies, we have removed the external aluminum shield of the rf probe to avoid large eddy currents induced by pulsed magnetic field gradients in conducting parts around the sample. Besides, glass inserts were also removed from the top part of the rf probe to avoid accidental damage. As it turned out later, another good reason to remove glass parts is their aluminum content (vide infra). The rf coil of the broadband probe inserted into the gradient set had its center ca. 6 mm lower than the isocenter of the gradient coils which presented no major problems for image detection.

The rf pulses for ^{27}Al NMR experiments were calibrated using an aqueous solution of $AlCl_3$. For the reduced rf power level used (10 db attenuation), the duration of the 180°-pulse was found to be equal to 60 μs. All imaging experiments were performed using the two-pulse spin–echo sequence.

$$\alpha\text{–}\tau\text{–}2\alpha\text{–}\tau\text{–echo} \quad (1)$$

with τ ca. 300 μs. For ^{27}Al experiments, the two pulses had the same amplitude and were 10 and 20 μs long, respectively, corresponding to the nominal flip angle $\alpha = 30°$. For other nuclei, the rf power was readjusted for maximum signal intensity ($\alpha = 45°$ for ^{23}Na, $\alpha = 22.5°$ for ^{51}V, vide infra).

In 2D imaging experiments, 64 complex data points of the echo signal were detected in the absence of a gradient, thus preserving in principle the spectroscopic information. The two spatial coordinates (x and y, transverse to the sample axis) were phase encoded by an independent stepwise variation of two pulsed transverse gradients G_X and G_Y (32 steps in the range −78 to 78 G/cm). The gradient pulses were 200 μs long and were applied during the first τ interval of Eq. (1). Before Fourier transformation, the two spatial dimensions were zero-filled to 256 data points each. A field of view $FOV_{XY} = (9.2\ \text{mm})^2$ was imaged with a true spatial resolution of $(288\ \mu\text{m})^2$ and a digital resolution of $(36\ \mu\text{m})^2$ obtained after zero filling. No slice selection was used.

In the 3D imaging experiments, the echo signal was frequency encoded along the Z axis ($FOV_Z = 24.5$ mm, $G_Z = 64$ G/cm) in addition to phase encoding in the XY plane ($G_X = G_Y$, 32 steps in the range −49 to 49 G/cm, $FOV_{XY} = (14.7\ \text{mm})^2$). The spatial resolution was $460 \times 460 \times 380\ \mu\text{m}^3$ (digital resolution after zero filling to 256^3 data matrix was $56 \times 56 \times 96\ \mu\text{m}^3$).

All ^{27}Al variable temperature and relaxation experiments were performed on a Bruker Avance DPX 200 MHz spectrometer at 52.1 MHz. The standard Bruker variable temperature accessory was used to set and maintain the required temperature with a flow of warm air. At each temperature setting, the equilibration delay of 20–30 min was used. In ^{27}Al saturation-recovery experiments, the following train of rf pulses was used for saturation:

$$(\Delta - \alpha_X - \Delta - \alpha_Y - \Delta - \alpha_{-X} - \Delta - \alpha_{-Y})_N, \quad (2)$$

with the nominal flip angle $\alpha = 30°$, interpulse delay $\Delta = 2$ ms and the number of repetitions $N = 16$. After

a variable recovery delay, the spin–echo sequence of Eq. (1) with $\tau = 45$ μs was applied and a single complex data point was detected at the echo maximum. Magnitude calculation was then performed on the time domain data points detected.

Alumina samples (γ-Al_2O_3) were from various batches and had different shapes (3.5 mm beads, cylinders 3.5 mm in diameter and ca. 1 cm long, powder). Cordierite monolith (400 cells per square inch) washcoated with alumina was received from Prof. D.O. Uner (Middle East Technical University, Ankara, Turkey). The channels have 1×1 mm^2 square cross-section and are separated by 0.3 mm walls. Small fragments which fit into the 6 mm i.d. saddle-shape rf coil were cut from the bigger original monolith along its channels. Baking soda, sodium chloride (both purchased at a local grocery store) and V_2O_5 powder were packed in the channels of such monolith fragments. In several experiments, Wilmad NMR tube (507-PP, borosilicate glass) with 5 mm outside diameter and wall thickness of 0.38 mm was used. In some experiments, alumina cylinders were degassed with a mechanical pump and flame-sealed in 5 mm Wilmad sample tubes.

3. The approach

A number of imaging strategies are employed to overcome substantial broadening of NMR resonances in solids. One of the approaches relies on an active line narrowing using sample rotation (e.g., magic angle spinning (MAS) with synchronized sample and magnetic field gradient rotation), multi-pulse line-narrowing sequences, and combination thereof [11–16]. Another general strategy to overcome substantial line broadening is based on the utilization of large static (e.g., in stray field imaging (STRAFI) [17–20]), pulsed [21,22] or oscillating [23,24] magnetic field gradients. Another possible course of action is the utilization of very short delays between the creation of the transverse magnetization and signal detection, sometimes in combination with rapidly oscillating gradients, or switching on the gradient before the excitation rf pulse and keeping it on while signal is detected, which forms the basis of most projection-reconstruction MRI studies [25,26]. Very short delays between excitation and detection are also used in constant time (CTI) and/or single point imaging (SPI) techniques [27–29] successfully employed for MRI of samples with short T_2 times. Other possibilities include continuous wave (in contrast to pulsed Fourier transform) MRI [30], the utilization of multiple quantum coherences [31,32] and the rotating frame imaging experiments which use gradients of the radiofrequency field [33,34].

While several research groups successfully develop the solids imaging strategies listed above, at present none of these applications can be considered a routine procedure since all these approaches require specialized (and often home-built) hardware. The ability to image rigid solids on a conventional imaging instrument might lead to a much broader interest and substantial progress in the imaging of solid materials. As a benchmark, we consider a commercial Bruker Avance DRX-300 WB system with imaging accessories (no sample rotation or translation, gradient amplitudes $\leqslant$40 or $\leqslant$100 G/cm, 200 kHz digitizer bandwidth, 100 W rf amplifier). Our choice of the solid matrix, γ-Al_2O_3 (and thus of the magnetic nucleus, ^{27}Al), was governed by our recent in situ MRI studies of the heterogeneous catalytic hydrogenation reaction of α-methylstyrene on Pt/γ-Al_2O_3 or Pd/γ-Al_2O_3 catalysts [35–37] as well as the fact that alumina is often used for supported catalysts preparation. Other nuclei that we consider here are ^{51}V of V_2O_5 and ^{23}Na of NaCl and $NaHCO_3$.

Our results rely on a number of well-established concepts. First, while the decay of transverse magnetization in solids is very rapid because of large line widths involved, in many cases this decay can be reversed to a significant degree using echo-type pulse sequences. In particular, the solid echo (90°_x–τ–90°_y–τ–echo), Hahn echo (90°–τ–180°–τ-echo) and other echo-based sequences [38–41] are often used to partially reverse the rapid decay of transverse magnetization in solids. This reversal is possible because the large broadening of NMR spectra in solids is inhomogeneous in nature. Next, for quadrupolar nuclei with half-integer spin including ^{23}Na ($I = 3/2$), ^{27}Al ($I = 5/2$), and ^{51}V ($I = 7/2$), central transition ($1/2 \leftrightarrow -1/2$) is broadened only to second order in perturbation theory [22,42]. This implies that relatively long rf pulses and limited digitizer bandwidth should be enough to excite and detect the central transition of these nuclei. The satellite transitions in the NMR spectra of quadrupolar nuclei are often too broad to be excited by the rf pulses a few microseconds long, thus only the central transition is excited and observed. In such a case, the optimum flip angle α in Eq. (1) is known to scale as $90^\circ/(I + 1/2)$ because of the higher nutation frequency of the magnetization associated with the central transition when the latter is excited selectively [43].

The limited amplitude of available gradients can make frequency encoding of spatial information problematic or impossible. Indeed, to be "resolved," two neighboring pixels of an image should differ in their resonance frequencies by an amount not less than the width of the detected NMR signal. Therefore, frequency encoding of the signal is of limited use for nuclei characterized by a large width of the central transition. The ^{23}Na resonances that we observe are ca. 4 kHz wide, which implies that a 100 G/cm gradient will allow one to obtain spatial resolution slightly better than 400 μm. For 12–14 kHz wide ^{27}Al resonances of

γ-Al_2O_3, the same gradient will limit the attainable resolution by 1.2 mm, which could still be acceptable in some applications. Larger broadening (e.g., ^{51}V, see below) will make frequency encoding useless. Fortunately, phase encoding is much more tolerant to large widths of NMR resonances. When MRI is performed in high magnetic fields, it is usually assumed that application of magnetic field gradients does not affect the orientation of the magnetic field $B = B_0 + \mathbf{G}_r\mathbf{r}$ and only makes its amplitude to depend on the spatial coordinate. In many cases, this assumption is justified and implies that unlike frequency encoding, the phase encoding of the signal is not sensitive to the broadening of the NMR resonances. Indeed, as demonstrated below, phase encoding allowed us to obtain true spatial resolution well below 1 mm for ^{27}Al MRI of γ-Al_2O_3. It should be noted, however, that for very large line broadening, even phase encoding approach can fail. For large quadrupolar coupling constants, the quantization axis of the nuclear spin is tilted away from the B_0 direction. This means that gradients creating fields perpendicular to B_0 ($dB_x/dz = dB_z/dx$) become important, and the resonance frequency becomes a complex function of both orientation and coordinate of the molecule. For broad resonances, rf pulses excite only certain molecular orientations. Correction terms broaden the resonance, with the extent of broadening depending of the sample size, which has been demonstrated for ^{63}Cu imaging of powdered Cu_2O [22].

It has been already pointed out in the literature that a 12 kHz wide central transition of ^{27}Al nucleus in alumina can be easily refocused using traditional spin echo methods, and that it should be possible to use ^{27}Al resonance of most ceramics to generate high-resolution spatial images [44]. A 1D image (projection) of a 6 mm ceramic cube or two such cubes separated with a spacer have been presented, albeit with a gradient (350 G/cm) larger than those available with routine systems, and an easy extension to multidimensional imaging has been noted [44]. There have been reports of one study where separate images of powdered alumina and zeolite samples were obtained [45,46], which seems to exhaust the examples of the multidimensional ^{27}Al imaging of solid materials. We believe that the progress in MRI techniques and applications during the last decade make further substantial advance in this field quite feasible.

The true power of MRI is its ability to provide parameter images, i.e., the ability to detect spatial distributions of a variety of object properties. In particular, NMR signal is sensitive to local temperature in the sample, which can be used for local temperature evaluation. In NMR spectroscopy, a number of chemicals (e.g., methanol, ethylene glycol) with known chemical shift temperature dependencies are used as temperature sensors. In biomedical MRI, temperature maps are obtained on the basis of the temperature dependence of the signal intensity, chemical shift, relaxation times and/or diffusivity of water and/or fat molecules in living organisms or phantom samples [2,47]. In all these cases, the NMR signal of a liquid or solute is detected. Therefore, none of these approaches is immediately and directly applicable to catalytic systems because all of the temperature sensitive parameters depend crucially on the degree of catalyst saturation with the liquid phase which can vary drastically during reactor operation.

It thus appears that NMR signal of the solid phase might be a better temperature sensor, equally applicable to gas–liquid–solid and gas–solid processes at elevated temperatures. However, the known applications of spatially resolved NMR thermometry to solid samples are predominantly limited to MRI of "soft" solids. A pronounced temperature dependence of the relaxation times (T_1, T_2) of such materials was used, for instance, to map temperature distributions within a block of *cis*-polybutadiene with imbedded hot and cold water pipes [48] and in SBR vulcanizates under dynamic mechanical load [5,6,49]. An example of NMR thermometry application to rigid solids is a 2D MRI study of KBr crystal [50]. The spin-lattice relaxation time T_1 of the ^{81}Br NMR signal was used as a temperature sensitive parameter, since in the absence of motional averaging T_2 exhibits no temperature dependence. A qualitative temperature map was detected while the sample was heated to about 313 K with a point heat source. For larger temperature ranges, signal intensity is another potential temperature sensor. These possibilities for ^{27}Al NMR thermometry are explored below.

4. Results and discussion

We begin with the discussion of multidimensional imaging of alumina catalyst supports using ^{27}Al NMR signal detection. Fig. 1 shows a 2D image of the cylindrical alumina pellet which appears in the image as a green inner circle. It is surrounded with a dark annulus with much lower signal intensity (walls of the sample tube, vide infra). The image took less than 18 min to acquire despite the fact that pure phase encoding was used for both spatial dimensions. The 1D cross-section through the center of the image shown above it demonstrates that the signal-to-noise ratio is reasonably high. No slice selection was performed in this experiment, therefore the projection of the entire pellet along its axis onto the image plane is observed. The pellets used in the experiments were not perfectly cylindrical and had visible surface defects. This reduces the steepness of the pellet image, as can be seen around the 2 O' clock position and at the right hand side of the 1D profile. Furthermore, an eight-fold zero-filling of the data set before Fourier transformation also adds some smoothness to the sharp boundaries. Despite that, the rest of the pellet

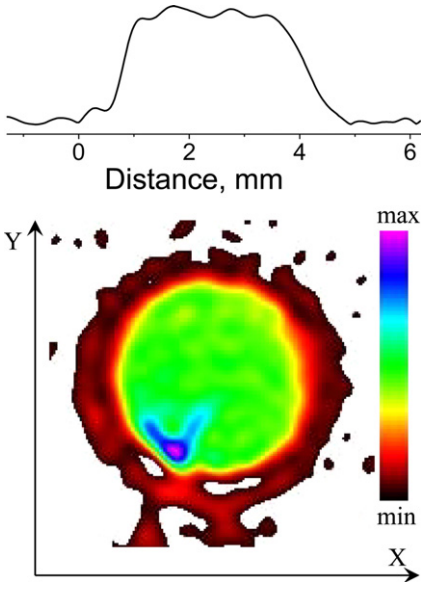

Fig. 1. Transverse two-dimensional ^{27}Al NMR image of a cylindrical γ-Al_2O_3 pellet in a 5 mm Wilmad NMR sample tube. Color bar shows signal intensity scale. 1D profile shown above the image represents its central horizontal cross-section. Image acquisition time was TA = 17.5 min, number of acquisitions NA = 2, pulse sequence repetition delay TR = 0.5 s.

boundary displays a steep signal change indicating that phase encoding for this sample is working quite well.

To demonstrate the feasibility of 3D imaging, we used several alumina beads placed in a 5 mm NMR tube in a single file. In this case, frequency encoding was used to encode the coordinate along the tube (Z), while phase encoding was employed for the other two dimensions. A 2D subset of the entire 3D image is shown in Fig. 2 along with its central 1D cross-section. The centers of the beads are not located on a straight line because the diameter of the beads (3.5 mm) is slightly smaller than the inner diameter of the sample tube (4.24 mm). The length of the sensitive region of the rf coil can be estimated from the extent of the visible area along the Z axis as ca. 12 mm. This leads to the observation of only four beads out of the entire much longer file used in the experiment. The 1D cross-section indicates that if frequency encoding is used, larger gradient strengths are likely to be needed in order to overcome the substantial line width for alumina samples, otherwise the features of an object under study are smeared out in the frequency encoding direction. The available gradient strength (100 G/cm) limits the spatial resolution in the frequency encoding direction to about 1.2 mm for alumina samples.

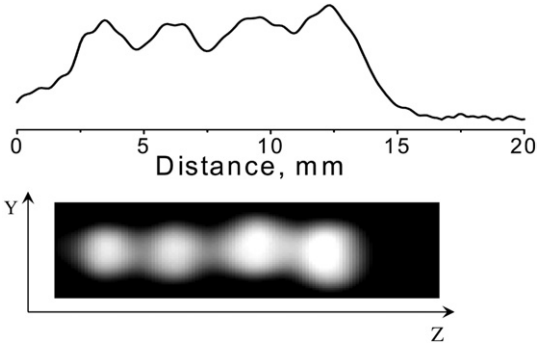

Fig. 2. One of the 2D cross-sections of a three-dimensional ^{27}Al NMR image obtained for γ-Al_2O_3 beads placed in 5 mm Wilmad NMR sample tube in a single file. Lighter shades of gray correspond to higher signal intensities. 1D profile shown above the image represents its central horizontal cross-section. TA = 11 h, NA = 64, TR = 0.6 s.

The results shown in Figs. 1 and 2 demonstrate that ^{27}Al MRI can be employed for the structural studies of packed beds and catalytic reactors which use alumina as a catalyst or catalyst support. In fact, the range of materials and processes that can be studied by ^{27}Al MRI is likely to be much broader than that. In particular, materials with much lower aluminum content, including various types of glasses and ceramics, can be successfully imaged with conventional imaging hardware. For instance, the low intensity annulus observed in the image of Fig. 1 has an external diameter of 5 mm, which suggests that it belongs to the Wilmad sample tube. The image shown in Fig. 3 which was obtained after removing the pellet from the sample tube leaves no doubt about it.

The v-shaped feature observed in the image of Fig. 3 as well as the signal present "inside" the tube originates from the rf probe itself. This was confirmed by running another experiment after removing the sample tube from the rf coil. We believe that the source of the ^{27}Al signal in the empty probe is a ceramic part located below the saddle-shape rf coil. While the upper edge of this

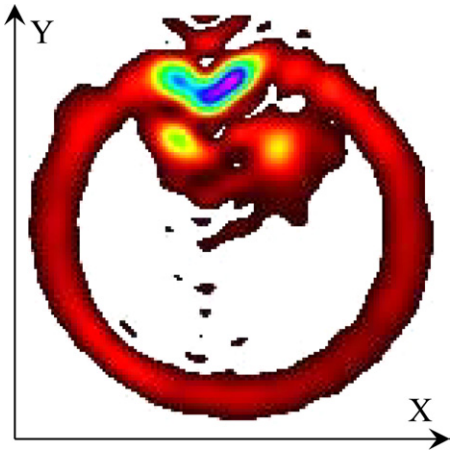

Fig. 3. Transverse two-dimensional ^{27}Al NMR image of a 5 mm o.d. Wilmad NMR sample tube which appears in the image as an annulus. The rest of the signal was shown to originate from the rf probe used in the imaging experiments. Lighter shades of gray correspond to higher signal intensities. In white areas, signal intensity is below the noise level. TA = 12.5 h, NA = 44, TR = 1 s.

ceramic part is located ca. 6 mm below the lower edge of the coil, the ceramic piece is large enough to produce a measurable signal despite a low rf field amplitude produced by the coil at its location.

Another example of the structural characterization of catalysts and catalyst supports by ^{27}Al MRI is presented in Fig. 4. A piece which fits into the rf coil with 6 mm i.d. was cut out of a cordierite monolith washcoated with alumina and imaged using phase encoding for both spatial dimensions. The aluminum content of cordierite is low (ca. 30% Al_2O_3), and the washcoat (γ-Al_2O_3) represents only ca. 14% of the sample mass. Higher signal intensity at the wall intersections and sample edges as well as other signal non-uniformities are caused by partial volume effects (wall thickness ca. 300 μm, spatial resolution 288 μm), inhomogeneity of the rf field of the saddle-shape coil, and the 8-fold increase in the number of points for each spatial dimension using zero-filling. Despite all these facts, the overall geometry of the monolith fragment as well as all its 12 square channels are well delineated.

While structural applications of the MRI technique are important, the main advantage of MRI is its ability to provide a wide range of properties of an object under study and processes which take place in it, based on the possibility to tailor the image contrast in MRI depending on the information required. For chemical engineering and catalytic applications it is highly desirable to characterize temperature fields in materials and operating reactors. Since the detection of ^{27}Al NMR signal of catalyst supports does not seem to be a problem, the temperature dependence of such signal can be used to evaluate local temperatures in aluminum-containing solid materials, in particular in catalysts. Of the parameters that are used for NMR thermometry in liquids, for alumina we have a priori discarded temperature dependent chemical shift (line widths too large) and diffusivity

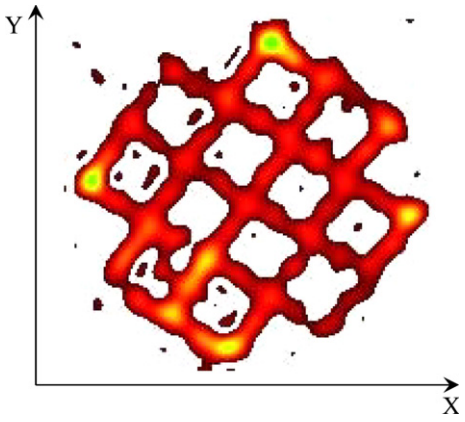

Fig. 4. Transverse two-dimensional ^{27}Al NMR image of a 400 cpsi cordierite monolith washcoated with alumina. Lighter shades of gray correspond to higher signal intensities. In white areas, signal intensity is below the noise level. TA = 2 h, NA = 64, TR = 0.1 s.

(values too low in solids). Our measurements at 4.7 T gave $T_2 = 1$–1.5 ms at room temperature and at 473 K. The differences in T_2 values at the two temperatures, if any [50], were smaller than the measurement accuracy achieved in these experiments. This leaves T_1 and NMR signal intensity as potential candidates for thermometry applications.

To test the possibility of using ^{27}Al NMR signal intensity and spin-lattice relaxation time T_1 as temperature sensitive parameters for NMR thermometry, we used cylindrical alumina pellets from the same batch as that imaged in Fig. 1. For these samples, saturation-recovery experiments were performed both at room temperature and at 473 K demonstrating that both the intensity of the signal after its complete recovery and the spin-lattice relaxation time decrease substantially as temperature increases. An accurate measurement of T_1 values requires the detection of the entire recovery curve, which is time consuming and thus can be impractical for measuring spatially resolved temperature maps. Besides, the recovery traces are not single-exponential. At room temperature, the bi-exponential fit yields $T_1^a \approx 16$ ms and $T_1^b \approx 1.9$ s with a 3:1 intensity ratio, while at 473 K it yields $T_1^a \approx 10$ and $T_1^b \approx 110$ ms. This further complicates an extraction of accurate values. It thus appears advantageous to measure NMR signal intensities, which can be done much faster. If the intensity of the signal is measured after a partial recovery, the information on the temperature dependent T_1 value will still be preserved and can be used to evaluate local temperatures.

We first discuss the temperature dependence of the intensity of the ^{27}Al NMR signal measured 2 s after its saturation, i.e., after its almost complete recovery. Triangles in Fig. 5A show the results of an automated spectrometer run in which sample temperature was stepped from low to high values and then back, with no probe tuning/matching except at room temperature. The ratio of signal intensities at two temperature values, I(300 K)/I(470 K), is 2.76, which by far exceeds the ratio of Boltzmann factors (1.577). Part of the difference is caused by the progressive probe mismatch as the temperature increases, leading to a more rapid apparent signal loss with increasing temperature. Therefore, in another experimental run, the probe tuning/matching was readjusted at each measurement temperature (Fig. 5A, circles and squares). In this case, the scatter of data for each temperature value increases reflecting the degree of readjustment reproducibility. The signal decrease with temperature becomes smaller, and the ratio I(299 K)/I(473 K) decreases to 2.08, which is still larger than expected for Boltzmann factor alone. One of the possible explanations is that since the echo with $T_E \approx 120$ μs is detected in these experiments, the signals are T_2-weighted, and thus slight temperature changes in T_2 will also contribute to temperature induced signal

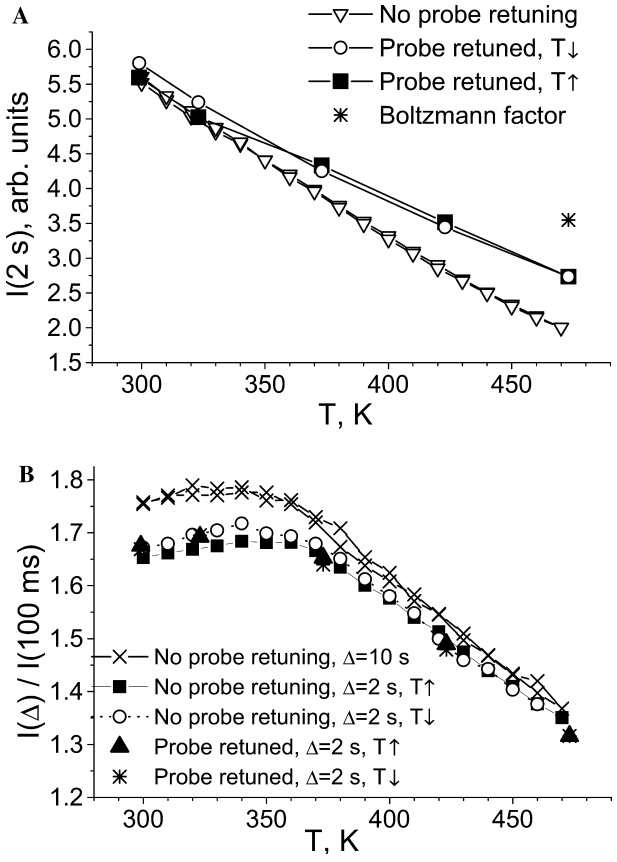

Fig. 5. (A) Temperature dependence of the ^{27}Al NMR signal of a cylindrical γ-Al_2O_3 pellet. The signal intensity was measured 2 s after the saturation cycle. The results of an automated variable temperature run (V) which was performed from low to high temperatures and then back, with no readjustment of the rf probe tuning/matching. In two other sets of experiments, the rf probe tuning/matching was manually readjusted for each temperature value, with temperatures changing in a descending (○) or ascending (■ order. An asterisk shows signal intensity estimated from the signal intensity at room temperature and Boltzmann factor change from RT to 473 K. (B) Temperature dependence of the ratio of the ^{27}Al NMR signals measured for γ-Al_2O_3 pellet at a relatively long delay Δ after saturation and at 100 ms. The results of the measurements for $\Delta = 2$ s for ascending (■, ▲) and descending temperatures (○, ∗) and with (▲, ∗) and without readjustment of probe tuning/matching (■, ○) fall more or less on the same curve, while the results of the experiment with $\Delta = 10$ s performed without probe tuning/matching readjustment for both ascending and descending temperatures (×) give larger values of the measured ratio. NA = 256.

variation. We believe, however, that the explanation should be sought in the changing number of ^{27}Al spins which contribute to the NMR signal (vide infra). In any case, the fact that the decrease of the signal with temperature is faster than expected from Boltzmann factor alone is advantageous since it provides higher temperature sensitivity, and can be accounted for by performing an appropriate calibration of signal intensity as a function of temperature (Fig. 5A).

At the same time, in certain cases signal intensity measurements for temperature evaluation purposes can be unreliable, e.g., due to the drift in hardware sensitivity (cf. Fig. 5A). In spatially resolved thermometry, small sample displacements can cause extra pixel intensity variations. Other possible sources of signal variations are plenty. Therefore, using two temperature dependent parameters for temperature evaluation can be more reliable than measuring signal intensity alone. Instead of using the T_1 value for reasons mentioned above, we use the ratio of signal intensities at long and short recovery delays, 2 s and 100 ms, respectively (Fig. 5B). As can be seen, this ratio exhibits a pronounced decrease with temperature above 340–360 K, i.e., in the region of interest for catalytic applications [35–37]. In the low temperature range (300–340 K) an opposite trend is observed, which at least partly is caused by the fact that recovery of the NMR signal for 2 s recovery delay is incomplete. When a longer recovery delay is used (10 s, crosses in Fig. 5B), the ratio becomes almost temperature independent in the range 300–340 K and decreases at higher temperatures.

Temperatures higher than 473 K were not accessible in experiments reported here. It is obvious, however, that the ratio of the completely recovered signal to the incompletely recovered one cannot be lower than unity. Therefore, somewhere at higher temperatures this ratio will once again become temperature independent. In that case, signal intensity at a delay shorter than 100 ms used here can be utilized. If a broad temperature range is of interest, several recovery delays with overlapping temperature sensitive regions can be useful.

While the variable temperature experiments reported above look promising, further research is needed to convert them into a practical tool for NMR thermometry. In particular, the NMR visibility of aluminas appears to be a non-trivial issue. It has been reported before that up to 45% of ^{27}Al nuclei can escape detection in static ^{27}Al NMR experiments performed on γ-alumina [51], while a later study claims that 100% of aluminum atoms contribute to the detected signal [52]. The existence of the correlation between aluminum visibility and sample surface area and the increase in line width of γ-alumina samples with increasing surface area, however, are not questioned. Therefore, the mechanism which determines visibility of aluminas appears to involve a number of dynamic processes on the surface where a highly distorted surrounding of aluminum atoms is expected to provide efficient quadrupolar relaxation pathways for surface Al atoms. These processes are able to affect 2–3 surface layers of aluminum atoms and thus can be quite important for γ-alumina samples with surface areas exceeding 200 m^2/g. Such dynamic processes can involve surface hydrogens and hydroxyls, adsorbed water and can be influenced by the presence of other adsorbates due to formation of new surface species as well as by temperature variations [51]. They can explain why signal intensity decrease with increasing temperature shown in Fig. 5A is

faster than the decrease in Boltzmann factor alone. Similar observation has been reported [51] when ^{27}Al NMR signals of γ-alumina were compared at 90 K and room temperature. In contrast, in another study no signal that was presumably lost due to surface dynamics could be regained by cooling the samples down to 173 K [52]. The NMR spectra of our γ-alumina samples reveal the presence of tetrahedrally and octahedrally coordinated Al atoms and are similar to those reported in the literature [51]. Therefore, in our studies dynamic processes on the alumina surface can be observable. Indeed, in some of the experiments it was noted that after the first two temperature cycles the overall signal intensity decreased noticeably, while further temperature cycles on the same sample gave almost identical temperature dependences of signal intensity. Condensation of water on the walls of the sample tube which originally was present in the alumina sample has been noticed in these experiments. For alumina pellets briefly vacuumed with a mechanical pump and sealed in a glass tube, no signal decrease in the initial temperature cycles was observed.

Finally, Fig. 6 shows a ^{51}V image of V_2O_5 powder packed in the channels of a cordierite monolith fragment identical to that shown in Fig. 4. The observed ^{51}V NMR spectrum of V_2O_5 is several times broader than the ^{27}Al spectrum of γ-Al_2O_3 and spreads over most of the 200 kHz receiver bandwidth of our NMR instruments. At the same time, spin-lattice relaxation time is relatively long, and the repetition time used ($T_R = 1$ s) was substantially shorter than $3T_1$. Despite that, phase encoding allows one to visualize the structure of the object under study. In particular, the channel walls are clearly observed which demonstrates that the true spatial resolution is high enough to resolve 300 μm features of the object under study. This example can be considered as a demonstration of the possibility to study other types of materials in general and catalysts in particular.

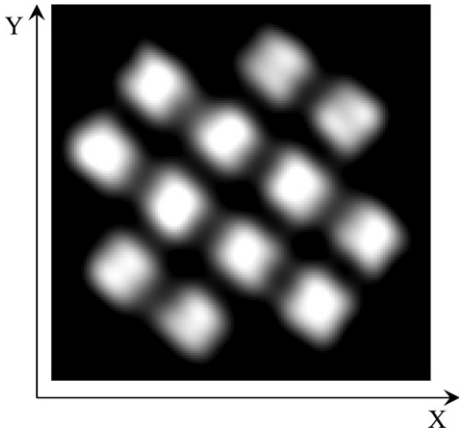

Fig. 6. Transverse two-dimensional ^{51}V NMR image of the 400 cpsi cordierite monolith with the channels packed with V_2O_5 powder. Lighter shades of gray correspond to higher signal intensities. TA = 18 h, NA = 64, TR = 1 s.

5. Conclusions and outlook

We have demonstrated that in certain cases, MRI of rigid solids does not require specialized solid state NMR hardware and can be performed on commercially available microimaging systems. In particular, ^{27}Al MRI appears to be a promising area of research. Potential applications of multidimensional ^{27}Al MRI and NMR thermometry in addition to catalytic applications cover a broad range of processes and applications involving aluminum containing ceramics. Besides, most natural and artificial glasses are aluminosilicates and thus can be studied using ^{27}Al NMR [53]. The possibility to detect half-integer nuclei other than ^{27}Al further broadens the scope of possible applications. Apart from results reported in this paper, other examples of materials and nuclei successfully imaged using the same instrument include glass (^{11}B, ^{23}Na, and ^{29}Si), silica gel (^{29}Si), NaCl (^{23}Na), and LiBr (^{7}Li) dispersed in alumina, alumina impregnated with phosphate (^{31}P), and chicken and fish bones (^{31}P) [54].

Furthermore, the information that can be obtained is not limited to structure only. Indeed, the utility of MRI is governed by the mechanisms and parameters which determine image contrast. In particular, this study demonstrates that both ^{27}Al NMR signal intensity and T_1 times of alumina exhibit a pronounced temperature dependence and thus can be considered as potential temperature sensors for the development of NMR thermometry applications. For materials science and chemical engineering as well as for catalytic applications, NMR thermometry based on the detection of the NMR signal of the solid phase can have distinct advantages over the conventional NMR thermometry approach with the detection of the signal of a liquid or solute. The experiments which combine ^{27}Al imaging and thermometry are currently in progress.

We hope that the results presented above will stimulate further studies in MRI of "rigid" solids and will lead to the development of novel applications of MRI to solid samples in a broad area of chemistry, engineering and technology. While several important issues, such as slice selection, 3D imaging, rapid imaging strategies and image contrast mechanisms other than spin density and temperature, were not addressed above, they are well documented in the solids imaging literature. Their implementation on a commercial microimaging instrument appears to be well within the reach.

Acknowledgments

The authors thank Alexandre V. Klotchkov (Kazan, Russian Federation) for useful suggestions. I.V. Koptyug and H. Van As acknowledge the RFBR-NWO grant (03-03-89014-NWO, 047.015.006), This work

was partially supported by the grants from RFBR (#05-03-32472), SB RAS (integration Grants ##41, 166), and the Russian President's program of support of the leading scientific schools (Grant # NSch-2298.2003.3). I.V. Koptyug thanks Russian Science Support Foundation for financial support.

References

[1] I.V. Koptyug, R.Z. Sagdeev, Russ. Chem. Rev. 71 (2002) 789.
[2] I.V. Koptyug, R.Z. Sagdeev, Russ. Chem. Rev. 72 (2003) 165.
[3] L.F. Gladden, Top. Catal. 8 (1999) 87.
[4] M.D. Mantle, A.J. Sederman, Prog. NMR Spectrosc. 43 (2003) 3.
[5] P. Blumler, B. Blumich, Rubber Chem. Technol. 70 (1997) 468.
[6] B. Blumich, P. Blumler, K. Saito, in: I. Ando, T. Asakura (Eds.), Solid State NMR of Polymers, Studies in Physical and Theoretical Chemistry, vol. 84, Elsevier Science, Amsterdam, 1998, pp. 123–163.
[7] A.N. Garroway, in: D.M. Grant, R.K. Harris (Eds.), Encyclopedia of Nuclear Magnetic Resonance, vol. 6, Wiley, Chichester, 1996, pp. 3683–3693.
[8] P. Jezzard, J.J. Attard, T.A. Carpenter, L.D. Hall, Prog. NMR Spectrosc. 23 (1991) 1.
[9] D.G. Cory, Annu. Rep. NMR Spectrosc. 24 (1992) 87.
[10] J.B. Miller, Prog. NMR Spectrosc. 33 (1998) 273.
[11] D.G. Cory, J.W.M. van Os, W.S. Veeman, J. Magn. Reson. 76 (1988) 543.
[12] D.G. Cory, J.B. Miller, R. Turner, A.N. Garroway, Mol. Phys. 70 (1990) 331.
[13] L.G. Butler, D.G. Cory, K.M. Dooley, J.B. Miller, A.N. Garroway, J. Am. Chem. Soc. 114 (1992) 125.
[14] W.S. Veeman, in: B. Blumich, W. Kuhn (Eds.), Magnetic Resonance Microscopy. Methods and Applications in Materials Science, Agriculture and Biomedicine, VCH, Weinheim, 1992, pp. 29–47.
[15] M. Buszko, G.E. Maciel, J. Magn. Reson. A 107 (1994) 151.
[16] D.E. Demco, R. Kimmich, S. Hafner, Meas. Sci. Technol. 2 (1991) 882.
[17] A.A. Samoilenko, D.Yu. Artemov, L.A. Sibeldina, JETP Lett. 47 (1988) 417.
[18] M.J.D. Mallett, M.R. Halse, J.H. Strange, J. Magn. Reson. 132 (1998) 172.
[19] P.J. McDonald, B. Newling, Rep. Prog. Phys. 61 (1998) 1441.
[20] E.W. Randall, in: D.M. Grant, R.K. Harris (Eds.), Encyclopedia of Nuclear Magnetic Resonance, vol. 9, Wiley, Chichester, 1996, pp. 150–165.
[21] W. Zhang, D.G. Cory, J. Magn. Reson. 132 (1998) 144.
[22] V.S. Swaminathan, B.H. Suits, J. Magn. Reson. 132 (1998) 274.
[23] S.L. Codd, M.J.D. Mallett, M.R. Halse, J.H. Strange, W. Vennart, T. Van Doorn, J. Magn. Reson. B 113 (1996) 214.
[24] P.J. McDonald, K.P. Perry, S.P. Roberts, Meas. Sci. Technol. 4 (1993) 896.
[25] J.M. Listerud, S.W. Sinton, G.P. Drobny, Anal. Chem. 61 (1989) 23A.
[26] B.H. Suits, D. White, Solid State Commun. 50 (1984) 291.
[27] S. Choi, X.-W. Tang, D.G. Cory, Int. J. Imaging Syst. Technol. 8 (1997) 263.
[28] S. Gravina, D.G. Cory, J. Magn. Reson. B 104 (1994) 53.
[29] B.J. Balcom, R.P. MacGregor, S.D. Beyea, D.P. Green, R.L. Armstrong, T.W. Bremner, J. Magn. Reson. A 123 (1996) 131.
[30] G.R. Davies, D.J. Lurie, J.M.S. Hutchison, S.J. McCallum, I. Nicholson, J. Magn. Reson. 148 (2001) 289.
[31] Garroway, J. Baum, M.G. Munowitz, A. Pines, J. Magn. Reson. 60 (1984) 337.
[32] B. Blumich, Concepts Magn. Reson. 11 (1999) 147.
[33] R. Kimmich, D.E. Demco, S. Hafner, in: B. Blumich, W. Kuhn (Eds.), Magnetic Resonance Microscopy. Methods and Applications in Materials Science, Agriculture and Biomedicine, VCH, Weinheim, 1992, pp. 59–83.
[34] F. De Luca, A. Gargaro, B. Maraviglia, G.H. Raza, C. Casieri, Magn. Reson. Imaging 16 (1998) 435.
[35] I.V. Koptyug, A.V. Kulikov, A.A. Lysova, V.A. Kirillov, V.N. Parmon, R.Z. Sagdeev, J. Am. Chem. Soc. 124 (2002) 9684.
[36] I.V. Koptyug, A.A. Lysova, A.V. Kulikov, V.A. Kirillov, V.N. Parmon, R.Z. Sagdeev, Appl. Catal. A: General 267 (2004) 143.
[37] V.A. Kirillov, I.V. Koptyug, A.V. Kulikov, N.A. Kuzin, A.A. Lysova, A.B. Shigarov, V.N. Parmon, Theor. Found Chem. Eng. 39 (2005) 24.
[38] P.J. McDonald, J.J. Attard, D.G. Taylor, J. Magn. Reson. 72 (1987) 224.
[39] B. Blumich, Concepts Magn. Reson. 11 (1999) 71.
[40] T. Gullion, D.B. Baker, M.S. Conradi, J. Magn. Reson. 89 (1990) 479.
[41] E. Rommel, S. Hafner, R. Kimmich, J. Magn. Reson. 86 (1990) 264.
[42] D.D. Laws, H.M.L. Bitter, A. Jerschow, Angew. Chem. Int. Ed. 41 (2002) 3096.
[43] A. Abragam, The Principles of Nuclear Magnetism, Clarendon Press, Oxford, 1961.
[44] M.S. Conradi, J. Magn. Reson. 93 (1991) 419.
[45] J.R. Moore, L. Garrido, J.L. Ackerman, Ceram. Eng. Sci. Proc. 11 (1990) 1302.
[46] J.L. Ackerman, L. Garrido, J.R. Moore, B. Pfleiderer, Y. Wu, in: B. Blumich, W. Kuhn (Eds.), Magnetic Resonance Microscopy. Methods and Applications in Materials Science, Agriculture and Biomedicine, VCH, Weinheim, 1992, pp. 237–260.
[47] N. Hosten, R. Felix, P. Wust, W. Wlodarczyk, M. Hentschel, R. Noeske, H. Rinneberg, Phys. Med. Biol. 44 (1999) 607.
[48] S.J. Doran, T.A. Carpenter, L.D. Hall, Rev. Sci. Instrum. 65 (1994) 2231.
[49] D. Hauck, P. Blumler, B. Blumich, Macromol. Chem. Phys. 198 (1997) 2729.
[50] B.H. Suits, D. White, J. Appl. Phys. 60 (1986) 3772.
[51] B.A. Huggins, P.D. Ellis, J. Am. Chem. Soc. 114 (1992) 2098.
[52] H. Kraus, M. Muller, R. Prins, A.P.M. Kentgens, J. Phys. Chem. B 102 (1998) 3862.
[53] F. Angeli, J.-M. Delaye, T. Charpentier, J.-C. Petit, D. Ghaleb, P. Faucon, Chem. Phys. Lett. 320 (2000) 681.
[54] I.V. Koptyug, A.A. Lysova, Bruker Spin Report, 2005 (accepted).